Eur. J. Mineral., 35, 831–844, 2023
https://doi.org/10.5194/ejm-35-831-2023

European Journal of Mineralogy
Open Access

Very-low-grade phyllosilicates in the Aravis massif (Haute-Savoie, France) and the di-trioctahedral substitution in chlorite

Benoît Dubacq[1,★], **Guillaume Bonnet**[1,★], **Manon Warembourg**[1], **and Benoît Baptiste**[2]

[1]Institut des Sciences de la Terre de Paris, ISTeP, UMR 7193, Sorbonne Université, CNRS-INSU, 75005 Paris, France
[2]Institut de Minéralogie, de Physique des Matériaux et de Cosmochimie, IMPMC, UMR 7590, Sorbonne Université, Muséum National d'Histoire Naturelle, CNRS, 75005 Paris, France
★These authors contributed equally to this work.

Correspondence: Benoît Dubacq (benoit.dubacq@sorbonne-universite.fr)

Received: 7 April 2023 – Revised: 23 August 2023 – Accepted: 25 August 2023 – Published: 4 October 2023

Abstract. Very-low-grade mineral veins investigated in the impure limestone massif of the Aravis (Haute-Savoie, France) yielded a rich mineral assemblage typified by dolomite, calcite, quartz, illitic mica, fluorite and three types of chlorite. The vein network extends over more than 5 km and was probably emplaced around peak burial of the limestone ($\sim$ 7 km depth, 190 °C). The mineralogy has been investigated with electron microscopy, mass spectrometry and X-ray diffraction, with emphasis on chlorite types. The first chlorite type is a chamosite often interlayered with illitic mica. The second type is a Mg-rich, Al-depleted cookeite. The third type is a Li-rich sudoite. Presence of the three chlorite types shows limited solubility between di-trioctahedral chlorite phase components (sudoite and cookeite) and with tri-trioctahedral chlorite (chamosite). Departure of the Li-rich sudoite and Mg-rich cookeite from the ideal end-member compositions suggests solid solutions towards a Li-sudoite component. The associated illitic mica does not contain Li in significant proportion but shows pyrophyllitic and di-trioctahedral substitution, without a Tschermak component. These results call for systematic studies of the Li content of chlorite and for better modelling of di-trioctahedral substitution in chlorite and mica.

1 Introduction

Chlorite is a common hydrous mineral of low-grade and very-low-grade metamorphism which may be found in metapelites, metabasalts, and altered granitoids and ultramafic rocks, as well as in impure limestones. Chlorite crystallizes during prograde or retrograde metamorphism, during hydrothermal alteration, and over a wide range of metamorphic grades. The composition of chlorite varies with crystallization conditions, in particular with temperature, and several models allow for using chlorite as a geothermometer. Some models link chlorite composition to crystallization temperature via empirical regression (e.g. Cathelineau, 1988; Inoue et al., 2009; Bourdelle et al., 2013a, b; Bourdelle and Cathelineau, 2015); some use thermodynamic modelling with solid solutions comprising variable sets of end-members (e.g. Walshe, 1986; Holland and Powell, 2003; Vidal et al., 2006; White et al., 2014; Lanari et al., 2014). All these models assume that chlorite composition evolves with temperature along solid solutions; however there is a profound divide in their handling of octahedral occupancy in particular.

Octahedral occupancy in low-temperature chlorite remains poorly known because of a lack of experimental results and of conflicting analyses on natural mineral assemblages, in addition to the difficulty of evaluating formula units in Fe-rich chlorite without measurement of the anionic basis, as highlighted by Masci et al. (2019).

The models of Vidal et al. (2006) and Lanari et al. (2014) allow modelling di-trioctahedral substitution in chlorite along an exchange of the type $3R^{2+} = 2R^{3+} + \square$, where $\square$ is an octahedral vacancy, using tri-trioctahedral clinochlore (ideally $Mg_5Al(AlSi_3)O_{10}(OH)_8$) and di-trioctahedral su-

doite (ideally $\square Mg_2Al_3(AlSi_3)O_{10}(OH)_8$) as end-members. These models assume strong non-ideality for the di-trioctahedral substitution, with a wide solvus between clinochlore and sudoite resulting in limited but increasing mutual solubility of the two end-members. The main observation backing presence of a solvus is frequent co-existence of sudoite with tri-trioctahedral chlorite. The models of Holland and Powell (2003) and White et al. (2014) exclude di-trioctahedral substitution. However, ultrafine measurements using TEM and/or synchrotron radiation by Bourdelle et al. (2013a, b) and Bourdelle and Cathelineau (2015) on the composition of low-grade chlorite resulted in all but complete solid solution between sudoite and tri-trioctahedral chlorite, with sudoite content apparently decreasing with increasing temperature. Drawing definitive conclusions over the thermodynamic properties of the di-trioctahedral substitution on the basis of these sole measurements remains unwise, firstly because reconstructing formula units from TEM analyses is notoriously difficult and estimating vacancy content cumulates analytical uncertainties. Secondly, there is a possibility that kinetics allows existence of metastable chlorite with intermediate octahedral occupancy in the samples of Bourdelle and co-authors.

Finding of chlorite in a network of veins in impure limestones of the Aravis massif (Haute-Savoie, France) allowed for studying an assemblage of three chlorite types in a simple context. Crystallization condition estimates are strongly constrained at a maximum of around 200 °C and 7 km burial by previous studies. The veins include chamosite (Mg–Fe chlorite with octahedral occupancy above 5.5 cations per $O_{10}(OH)_8$ formula unit), cookeite (a di-trioctahedral chlorite with ideal composition $\square LiAl_4(AlSi_3)O_{10}(OH)_8$) and sudoite, together with carbonate, quartz, illitic mica and fluorite. These rocks provide an ideal opportunity for a case study of the extent of solid solutions in low-temperature chlorite. A combination of analytical techniques has been used to ensure that all cations in major concentration have been measured in situ, including light elements (Li, Be, B). The structure of the sudoite has been studied with X-ray diffraction to ensure identification.

2 Geological setting

The Aravis massif is part of the subalpine massifs from the Western Alps, composed of a series of sedimentary nappes in a chain of fold-and-thrust structures. The north-eastern part of the Aravis massif studied here is made of sedimentary rocks, including limestone, shale and sandstone of varying purity, spanning ∼ 150 My of deposition of sediments from Toarcian (Early Jurassic) to Rupelian (early Oligocene).

Nappe tectonics were active as early as the Oligocene (e.g. Dumont et al., 2008) during which the Aravis massif was buried under the Prealpine nappes of more internal origin (now mainly observed in the Chablais and Romand Prealps).

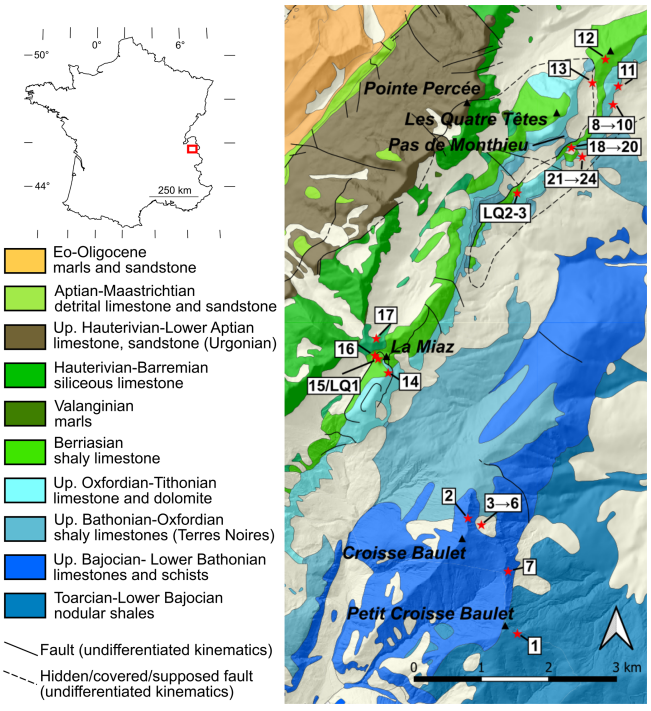

Figure 1. Sample location over geological map with topographic shading, after Pairis et al. (1992a). The inset shows the location of the Aravis massif. Sample labels with numbers only are abbreviated from the prefix "AR21-" for readability.

In the Aravis massif, remains of this nappe are the Annes and Sulens klippes, thrust over Rupelian clastic sediments ("Grès de Taveyannaz"). Compressional tectonics continued until Late Miocene times, associated with exhumation of the external crystalline massifs including the Mont Blanc massif (see Bellahsen et al., 2014, for a review). Tectonic reconstructions and palaeothermometric data showed that the subalpine massifs were buried below the Prealpine nappe to increasing depths to the north-east, in a relatively warm geothermal gradient around 28 °C km^{-1} (Butler, 1991; Moss, 1992; Deville and Sassi, 2006; Mangenot et al., 2019; Muirhead et al., 2020). For Hauterivian–Aptian sediments now constituting the main ridge of the Aravis massif (Urgonian-facies limestone), this resulted in peak burial around 7 km (i.e. about 0.2 GPa) at a temperature of 190 °C (±20 °C depending on studies) in Miocene times.

2.1 Study site and description of samples

The study site is located east and south of Pointe Percée, the highest point of the massif (Fig. 1). There, north-west-dipping Urgonian-facies limestone makes up the summits and conformably overlays older sediments down to the Terres Noires formation. A north-west-dipping thrust best observed near Pas de Monthieu locally duplicates the sedimentary section from the Terres Noires formation up to Berriasian-age

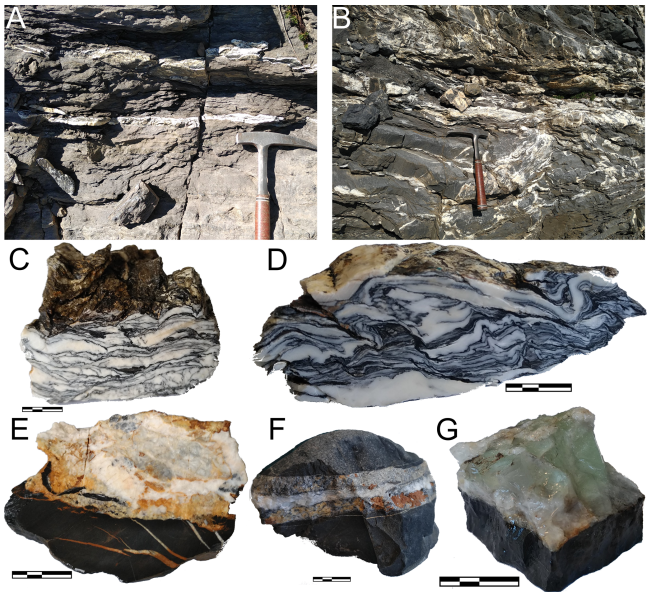

Figure 2. Photographs of representative outcrops and samples. **(a, b)** The vein network in shaly limestones of Berriasian age (**a**, between locations of samples 16 and 17 north-west of La Miaz) and of Oxfordian age (**b**, Argovian facies near Pas de Monthieu). **(c–e)** Close-up views of macroscopic samples. Panels **(c)** and **(d)** show deformed calcite–mica–chlorite–quartz veins found parallel to the bedding (**c**: LQ1, in Berriasian limestone – see also Fig. 3c; **d**: AR21-18b in Oxfordian limestone). Panels **(e)** and **(f)** show calcite–dolomite–ankerite–chlorite–quartz veins in Oxfordian limestone, parallel to the bedding (**e**: LQ3 – see Fig. 3d; **f**: AR21-22b). Panel **(g)** shows green fluorite–calcite–dolomite veins with minor chlorite in Oxfordian limestone (AR21-21, Fig. 3e). In **(c)** to **(g)**, the scale bar is 2 cm long in total.

sediments. The thrust propagates to the south-west to the summit of La Miaz, where thrusting increases the apparent thickness of the Berriasian shaly limestone. Further south, the summit of Croisse Baulet shows spectacular synformal and antiformal folding into Jurassic limestone.

A discrete yet extensive network of carbonate-bearing veins was noticed and sampled near the summits of Croisse Baulet and La Miaz and followed to the north-east through the Pas de Monthieu. The veins, generally white or pale grey, are in striking contrast with the host rock, especially in the dark Jurassic Terres Noires at the base of Croisse Baulet, near Pas de Monthieu and Valanginian marls near La Miaz. The veins vary in thickness between a few and about 50 cm. They propagate along the bedding (Fig. 2a) and can be followed over hundreds of metres (exposure permitting). Near the thrust at Pas de Monthieu, the vein network is in greater proportion to the host rock and veins often cross-cut the bedding at sharp angles (Fig. 2b). These veins appear chaotic near the thrust at Pas de Monthieu but are dominantly subvertical and aligned to N130 fractures, parallel to a set of small faults reported on the geological map (Fig. 1).

The mineralogy of the veins is similar at all sites, although mineral modes vary between samples. Typical samples are shown in Fig. 2c–g. Carbonates are dominant with calcite (locally with crystals exceeding 20 cm), dolomite and ankerite often altered to hematite, giving it a rusty colour. Quartz is ubiquitous in generally millimetric crystals. Phyllosilicates make thin, dark layers revealing deformation (e.g. Fig. 2c–d); these layers include minute mica and chlorite that are often interlayered and hard to resolve. Fluorite has been found as microscopic crystals at Croisse Baulet and La Miaz and in centimetric crystals near Pas de Monthieu, where it has already been reported in large fallen boulders (at least since Rosset, 1954) and where it is locally known by mineral enthusiasts for its green colour (Fig. 2g; see historical reconstruction by Féraud, 2021, unreviewed publication). Rosset linked the Aravis fluorite to earlier reports of fluorite in Urgonian-facies limestone near the summit of the Petit Salève (37 km away but with comparable geological history) by Lacroix (1896, p. 793) and Soret (1822, p. 476). Fluorite is also found on the north-west-dipping slabs of Les Quatre Têtes (Fig. 1) in veins parallel to the N130 faults. Sulfides consisting mostly in pyrite and chalcopyrite are found in scattered veins mostly at the Pas de Monthieu and Petit Croisse Baulet sites.

The host rocks are limestones of varying purity, from the shaly schistose limestone of the Terres Noires formation to the much purer Titonian limestone making up the summit of La Miaz. Clay minerals are often abundant in the host rocks, together with detrital minerals (e.g. Pairis et al., 1992b). Clasts of host rocks appear in the veins (e.g. Fig. 2e) without clear evidence of transport over distances greater than vein width.

3 Analytical methods

Samples of veins selected for their representative mineralogy as well as samples from the various host rocks have been analysed in situ for major element composition by electron microscopy and by mass spectrometry for light elements, over carbon-coated thin and thick sections. Samples were selected for analysis on the basis of the size of individual crystals; in particular laser-ablation mass spectrometry could not be carried out over all phyllosilicates due to beam size. The structure of one type of chlorite has been investigated to ensure identification and the correct formula unit.

3.1 Electron microscopy and chemical analysis

Scanning electron microscopy (SEM) was carried out after optical microscopy at the Institut des Sciences de la Terre de Paris (ISTeP, Sorbonne Université, Paris, France) using a Zeiss Supra 55VP apparatus with a field emission gun (FEG) associated with a PTG Sahara solid-state detector, for imaging with backscattered electrons (BSEs) and elemental map-

ping in energy-dispersive spectroscopy (EDS) mode. The SEM is also equipped with an OPEA cathodoluminescence apparatus using parabolic mirror guiding luminescence towards a photomultiplier for imaging. Careful EDS measurements ensured that no unexpected elements heavier than boron were present in significant concentration in the minerals. Electron probe microanalyses (EPMAs) were carried out at CAMPARIS (Sorbonne Université, Paris, France) with both Cameca SXFive and Cameca SX 100 instruments. Point measurements were obtained in classical analytical conditions (15 kV acceleration voltage and 10 nA beam current allowing ~ 1.5 µm beam size in wavelength-dispersive spectroscopy mode) using diopside (Ca, Mg, Si), $MnTiO_3$ (Mn, Ti), orthoclase (K, Al), Fe_2O_3 (Fe), albite (Na) and Cr_2O_3 (Cr) as standards for calibration of elements in parentheses. Analyses were calibrated with the manufacturer's software using the method of Pouchou and Pichoir (1994). EPMA allowed measurement of most crystals of interest, with the exception of some finely interlayered chlorite and mica which yielded mixed compositions (discarded).

Light elements (Li, Be and B) were measured from trace to major concentrations with laser-ablation mass spectrometry (LA MS) at the ALIPP6 facility (ISTeP, Sorbonne Université, Paris, France) using an Agilent 8900 inductively coupled plasma tandem mass spectrometry (ICP-MS/MS) instrument coupled to a Teledyne Analyte G2 193 nm ArF excimer laser-ablation system. Crystals and crystal aggregates of all chlorite types, mica and fluorite were ablated for 60 s (at a frequency of 8 Hz) under He fluxing using a 30 µm beam and a laser fluency of $3.54\,J\,cm^{-2}$. Background was measured 18 s before and after sampling ablation. Standardization was carried out using international standards ATHOG, BIR-1G, BCR-2G and BHVO-2G and in-house standard HAM. Calcium at mass 43, ^{39}K, ^{28}Si, ^{24}Mg, ^{23}Na, ^{57}Fe and ^{27}Al were also measured to ensure homogeneity of the ablated material and for use as internal standards obtained from electron microprobe analyses. Instrument drift and accuracy were controlled with repeated analyses of all standards. Each ablation pattern has been verified with an in-house spreadsheet to check for absence of impurities and/or inclusions during ablation. Cookeite from the study of Verlaguet et al. (2011) was measured as a secondary standard to ensure correct extrapolation to high-Li contents, yielding 2.83 wt % Li_2O in analyses with $Al/Si = 1.66$ close to ideal cookeite, for an ideal Li_2O concentration of 2.86 wt %, validating calibration. As individual chlorite crystals were often smaller than beam size, ablation has been carried out in aggregates including several crystals of identical type and homogenous composition. In the case of interlayered chlorite–mica aggregates, in most cases they were too small for ablation of individual mineral types. In these cases, interlayered chlorite–mica aggregates were measured as a whole to check for possibly high light-element content from the ablation pattern. No measurement revealed light-element enrichment in a range possibly above 50 ppm; therefore it was concluded that these interlayered chlorite–mica aggregates do not include light elements in significant proportions, without proceeding further towards internal standardization, which was made difficult by phase mixing. For this reason the corresponding LA ICP-MS/MS analyses are not reported.

It was found that the vein samples show varying mineral compositions but with high intra-sample homogeneity. Therefore, EPMA mineral compositions have been averaged, mineral type per mineral type and sample per sample, when possible and relevant. This allowed for internal standardization of LA ICP-MS/MS analyses.

Formula units are reconstructed from averaged mass proportions measured with EPMA and LA ICP-MS/MS, assuming 28 charges for chlorite and 22 for mica. Uncertainties have been estimated from the combination of analytical uncertainty and spread of the measured compositions, the latter being the largest source of uncertainty. To do so, a Monte Carlo simulation has been carried out for each analysis, using the standard deviation of estimated quantities from a synthetic pseudo-random dataset of 100 analyses drawn within uncertainties of the original dataset. This has been preferred over analytical error propagation, which is rendered tedious by correlation of variables during normalization to fixed-charge bases, leading to over-estimation of uncertainties if unaccounted for. Contents in Be and B revealed below 50 ppm for all analyses and are not reported, which is the same as for fluorite measurements, which revealed Li content below 20 ppm after calibration to ideal CaF_2 composition.

3.2 X-ray diffraction

Due to difficulties in extracting sufficient quantities of sudoite crystals from calcite and dolomite, X-ray diffraction (XRD) has been carried out directly over a ~ 100 µm thick section of sample LQ3. The section has been polished on both sides and prepared over standard thin-section glass glued with cyanoacrylate resin. The entire section has been recovered from the glass after 2 d of dissolution of the cyanoacrylate resin in acetone and then carefully rinsed for residues. The section has subsequently been analysed with SEM without carbon coating, allowing recognition of areas suitable for XRD (Fig. 4a).

Laboratory X-ray diffraction experiments were performed at the X-ray diffraction facility of the Institut de Minéralogie, de Physique des Matériaux et Cosmochimie (IMPMC, Sorbonne Université, Paris, France). A Rigaku MM007HF diffractometer equipped with Varimax focusing optics, a RAXIS4++ image plate detector ($30 \times 30\,cm^2$) placed at a distance of 300 mm from the sample, and a Mo rotating anode ($\lambda K\alpha 1 = 0.709319$ Å and $\lambda K\alpha 2 = 0.713609$ Å) at 50 keV and 24 mA were used. With this geometry, the measured 2θ range varied between 2 and 35°. Regions of interest were analysed with a micro-focused and low divergent X-ray beam (80 µm full width at half maximum) in transmission geometry with an exposure time of 45 min, constantly rotat-

ing the thin section over 40° in the horizontal direction. The *FIT2D* program (Hammersley, 2016) was used for integration of 2D images into 1D patterns after calibration using a LaB_6 crystal standard. The *FullProf* program (Rodríguez-Carvajal, 1993) was used for data reduction and modelling.

4 Results

Table 1 lists results from chemical analyses on chlorite and Table 2 those from chemical analyses on mica.

4.1 Phyllosilicate mineralogy

Five types of phyllosilicates have been identified. Micas include paragonite and a dioctahedral K-deficient mica referred to as illitic mica (see Meunier and Velde, 1989; Abad et al., 2006; Dubacq et al., 2010). Chlorite types consist in Fe-rich chlorite close to chamosite, cookeite and sudoite. All are found in the veins. The host rocks include illitic mica, paragonite and chamosite, among detrital minerals. Sudoite has been found in the host rock in the close vicinity ($\sim$ 1 cm) of veins or veinlets; cookeite has not been observed in the host rocks.

Figure 3 shows microscopic views of the textural relationships in the veins, focusing on phyllosilicates. Sudoite is found filling infra-millimetric cavities between spearhead dolomite crystals with calcite (Fig. 3a–b) and as small individual crystals in the dark phyllosilicate-rich layers bearing interlayered chamosite–illitic mica aggregates (Fig. 3d). The sudoite crystals are colourless and translucent under the optical microscope with low birefringence and straight extinction. They appear homogenous at least at centimetric scale and are in the range of 5–25 µm (e.g. Fig. 3c). Sudoite is also found co-existing with quartz (Fig. 3f–g) and fluorite (Fig. 3g), as well as in samples bearing calcite–cookeite veinlets (Fig. 3i). Cookeite appears as fibrous crystals up to 0.5 mm in size, growing with quartz, fluorite, coarse-grained calcite and dolomite (Fig. 3h), sometimes with fibroradial structure (associated with a calcite veinlet in Fig. 3i). Newly formed (i.e. not detrital) chamosite and illitic mica are abundantly found in dark layers of veins (Figs. 2c–d, 3d) and in the host rock apart from pure limestone, for example in Jurassic Terres Noires and Valanginian marls. Quartz and carbonate are ubiquitous. Dolomite crystals appear as early phases in the veins, often dismembered and cross-cut by calcite. There are at least three calcite generations: coarse-grained calcite apparently growing with dolomite is followed by fine-grained calcite and by calcite veinlets (Fig. 3a–b, f–g, i). Poikilitic calcite is found enclosing euhedral quartz with interstitial sudoite (Fig. 3f). The calcite is very weakly cathodoluminescent; euhedral quartz grains show stronger cathodoluminescence, revealing sector zoning, a feature classically associated with out-of-equilibrium growth and consistent with rapid growth (e.g. Dowty, 1976; Van Hinsberg et al., 2006).

Figure 4 summarizes results obtained by X-ray diffraction carried out for identification of the Li-rich chlorite. The Li-rich chlorite is confidently confirmed as pure (not interlayered with a mica-like mineral) and of sudoite type, with strong $hkl = 003$ (4.7 Å) and 111 (4.4 Å) reflections as in the reference study of Eggleton and Bailey (1967) and less intense $hkl = 001$ (14 Å) and $hkl = 002$ (7 Å) reflections classically associated with chlorite. Peak broadening appeared higher than instrumental resolution, indicating microstrain, stacking faults or disorder as reported in Fe-rich chlorite (Walker and Bish, 1992). The 2D diffraction pattern (Fig. 4b) revealed some preferential orientation, as all the Debye rings are not continuous. Moreover, absent or poorly defined Bragg peaks between 10 and 15° 2θ (i.e. 2.7 Å $< d <$ 4.10 Å) confirm layer stacking disorder. Consequently, Rietveld refinement attempts proved unsatisfying as preferential orientation could not be meaningfully disentangled from the structural model where cation distribution is uncertain. Le Bail fitting was performed, starting from the unit cell parameters of sudoite (space group: *C*2/*m*, as in Eggleton and Bailey, 1967) and leading to the results presented in Fig. 4d. Presence of a broad diffuse peak around 3° 2θ has been attributed to residues of hardening resin and cyanoacrylate used for sample preparation and has been treated as background. Importantly, this feature does not compromise identification of chlorite (14 Å peak at lower angle, Fig. 4d) or muscovite (10 Å peak around 4° 2θ), not found here. Cell parameters obtained for the Li-rich sudoite are $a = 5.219(3)$ Å, $b = 8.922(6)$ Å, $c = 14.282(9)$ Å and $\beta g = 96.90(5)°$.

4.2 Chlorite chemistry

To distinguish chlorite types without assumptions about the anionic basis, elemental ratios are reported in Fig. 5a from EPMA results with elements grouped per valence ($R^{2+} = Mg + Fe^{2+}_{TOT}$; $R^{3+} = Al + Cr$; $R^{4+} = Si + Ti$, using molar proportions). This allows for estimating end-member proportions in favourable cases. The dependency on iron speciation has been tested for each chlorite composition, unsurprisingly resulting in strong sensitivity of sudoite content for Fe-rich chlorite (arrows in Fig. 5a). Sudoite and cookeite composition estimates are insignificantly affected by iron speciation.

Chamosite has variable composition but with invariably low X_{Mg} in the range of 0.35–0.50 (using $X_{Mg} = Mg^{2+} / (Fe^{2+}_{TOT} + Mg^{2+})$ with all Fe assumed divalent). It is noted that variations in iron speciation will significantly affect formula unit estimations in this chlorite (Fig. 5a) and that assumptions over anionic basis with 28 charges may be erroneous (see Masci et al., 2019). Therefore, chamosite formula units in Table 1 remain little more than indicative. Chamosite appears as a possible solid solution between trioctahedral chlorite components (of clinochlore and ame-

https://doi.org/10.5194/ejm-35-831-2023

Table 1. Composition of chlorites measured in this study, averaged over the number of analyses given in the second line. Laser-ablation ICP-MS analyses are only used for Li. Lithium could not be measured when crystals were too small for measurement; in cases where Li is suspected, oxide weight percent totals are written in italics and formula units are uncertain due to normalization biases. Dash: not measured; "b.d.l.": below detection limits.

Sample	LQ1						LQ1-bis		LQ2		LQ3a		AR21-01			
Mineral (n analyses)	Chm. ($n_{EPMA} = 2$)		Chm. ($n_{EPMA} = 3$)		Sud. ($n_{EPMA} = 14$)		Sud. ($n_{EPMA} = 11$)		Cook. ($n_{EPMA} = 14$, $n_{LA\text{-}ICP} = 3$)		Sud. ($n_{EPMA} = 10$, $n_{LA\text{-}ICP} = 6$)		Chm. ($n_{EPMA} = 5$)		Chm. ($n_{EPMA} = 12$)	
Composition (ox. wt %)																
SiO_2	27.02	(1.78)	28.14	(0.6)	35.37	(0.61)	34.94	(0.51)	36.49	(0.42)	36.95	(1.32)	23.20	(0.78)	24.86	(0.78)
TiO_2	0.014	(0.003)	0.049	(0.024)	0.028	(0.035)	0.018	(0.018)	b.d.l.	0.00	0.008	(0.021)	0.026	(0.023)	b.d.l.	
Al_2O_3	25.72	(0.32)	26.35	(0.75)	35.72	(1.03)	35.13	(0.44)	47.02	(1.59)	37.69	(1.79)	22.54	(0.88)	24.07	(0.75)
Cr_2O_3	0.027	(0.015)	0.033	(0.009)	0.014	(0.034)	0.026	(0.021)	b.d.l.		0.031	(0.049)	b.d.l.		b.d.l.	0.00
FeO	25.68	(1.9)	21.78	(1.67)	5.83	(0.53)	6.24	(0.78)	0.14	(0.05)	3.10	(0.45)	33.28	(0.82)	28.21	(1.73)
MnO	b.d.l.		b.d.l.		b.d.l.		b.d.l.		b.d.l.		b.d.l.		0.020	(0.035)	0.09	(0.052)
MgO	7.83	(0.99)	11.20	(0.59)	10.53	(0.33)	10.45	(0.31)	0.66	(0.15)	9.54	(1.73)	6.66	(0.53)	9.96	(1.15)
CaO	0.12	(0.09)	0.14	(0.02)	0.13	(0.035)	0.18	(0.056)	0.070	(0.045)	0.190	(0.097)	0.086	(0.065)	0.05	(0.056)
Na_2O	0.11	(0.12)	0.092	(0.045)	0.23	(0.17)	0.078	(0.063)	0.024	(0.022)	0.114	(0.054)	0.038	(0.038)	0.02	(0.03)
K_2O	0.13	(0.11)	0.15	(0.1)	0.167	(0.096)	0.091	(0.063)	0.012	(0.011)	0.26	(0.17)	0.02	(0.03)	0.09	(0.12)
Li_2O	–		–		–		–		2.54	(0.14)	0.479	(0.069)	–		–	
Total	86.65		87.95		*88.02*		87.15		86.97		88.37		85.89		87.39	
Formula with 28-charge basis																
Si	2.84	(0.11)	2.85	(0.05)	*3.19*	*(0.05)*	3.19	(0.03)	3.15	(0.06)	3.26	(0.1)	2.61	(0.06)	2.66	(0.07)
Ti	< 0.01		< 0.01		*<0.01*		< 0.01		b.d.l.	0.00	< 0.01		< 0.01		b.d.l.	
Al	3.19	(0.09)	3.15	(0.07)	*3.80*	*(0.07)*	3.78	(0.04)	4.78	(0.08)	3.92	(0.14)	2.99	(0.09)	3.03	(0.09)
Cr	< 0.01		< 0.01		*<0.01*		< 0.01		b.d.l.		< 0.01		b.d.l.		b.d.l.	
Fe^{2+}	2.26	(0.14)	1.85	(0.11)	*0.44*	*(0.03)*	0.48	(0.05)	0.01	(0.004)	0.23	(0.03)	3.14	(0.09)	2.52	(0.13)
Mn	b.d.l.		b.d.l.		*b.d.l.*		b.d.l.		b.d.l.		b.d.l.		< 0.01		< 0.01	
Mg	1.23	(0.15)	1.69	(0.08)	*1.42*	*(0.04)*	1.42	(0.04)	0.09	(0.02)	1.25	(0.2)	1.12	(0.08)	1.59	(0.17)
Ca	0.01	(0.01)	0.02	(0.002)	*0.01*	*(0.003)*	0.02	(0.005)	< 0.01		0.02	(0.009)	0.01	(0.008)	< 0.01	
Na	0.02	(0.02)	0.02	(0.007)	*0.04*	*(0.03)*	0.01	(0.01)	< 0.01		0.02	(0.009)	< 0.01		< 0.01	
K	0.02	(0.02)	0.02	(0.01)	*0.02*	*(0.01)*	0.01	(0.006)	< 0.01		0.03	(0.02)	< 0.01		0.01	(0.02)
Li	–		–		–		–		0.88	(0.05)	0.17	(0.02)	–		–	
Cation sum	9.58	(0.1)	9.59	(0.05)	*8.93*	*(0.04)*	8.92	(0.03)	8.91	(0.03)	8.89	(0.09)	9.89	(0.05)	9.83	(0.07)
Octahedral sum	5.58	(0.1)	5.59	(0.05)	*4.93*	*(0.03)*	4.92	(0.03)	4.91	(0.03)	4.89	(0.09)	5.89	(0.04)	5.83	(0.07)

Table 1. Continued.

AR21-02 Chm. ($n_{EPMA} = 2$)		AR21-03 Chm. ($n_{EPMA} = 3$)		AR21-06B Chm. ($n_{EPMA} = 13$)		AR21-10 Sud. ($n_{EPMA} = 9$, $n_{LA\text{-}ICP} = 12$)		AR21-15 Cook. ($n_{EPMA} = 9$, $n_{LA\text{-}ICP} = 2$)		AR21-18B Chm. ($n_{EPMA} = 6$)		AR21-20 Sud. ($n_{EPMA} = 9$, $n_{LA\text{-}ICP} = 3$)		AR21-21 Cook. ($n_{EPMA} = 4$)		AR21-22 Sud. ($n_{EPMA} = 3$, $n_{LA\text{-}ICP} = 2$)		AR21-24 Cook. ($n_{EPMA} = 5$)	
Composition (ox. wt %)																			
28.34	(0.53)	25.26	(1.24)	26.62	(0.49)	36.15	(0.42)	36.90	(0.37)	28.84	(0.94)	35.48	(0.9)	36.18	(0.72)	36.09	(1.61)	37.06	(0.57)
b.d.l.	0.00	0.01	(0.016)	0.011	(0.025)	b.d.l.		b.d.l.		0.02	(0.02)	b.d.l.		b.d.l.		0.021	(0.013)	0.021	(0.019)
23.66	(0.1)	23.35	(0.51)	24.08	(0.48)	36.54	(0.65)	46.58	(0.54)	25.12	(1.18)	34.58	(0.65)	45.14	(0.86)	34.83	(1.06)	47.15	(0.63)
0.044	(0.007)	0.01	(0.04)	0.023	(0.034)	b.d.l.		b.d.l.		0.021	(0.016)	b.d.l.		0.06	(0.03)	0.040	(0.019)	0.026	(0.024)
14.71	(0.22)	22.10	(0.48)	21.63	(0.7)	1.88	(0.32)	0.22	(0.092)	17.52	(1.35)	4.12	(1.05)	0.25	(0.12)	1.47	(0.27)	0.361	(0.043)
0.011	(0.016)	0.01	(0.008)	b.d.l.		0.028	(0.028)	b.d.l.		b.d.l.		b.d.l.		0.018	(0.015)	b.d.l.		b.d.l.	
18.58	(0.48)	13.83	(0.65)	13.41	(0.33)	12.70	(0.8)	0.72	(0.18)	16.71	(0.46)	12.14	(0.52)	0.697	(0.082)	12.10	(1.16)	0.96	(0.16)
0.137	(0.045)	0.08	(0.016)	0.07	(0.05)	0.100	(0.055)	0.157	(0.037)	0.190	(0.052)	0.14	(0.11)	0.431	(0.055)	0.265	(0.021)	0.114	(0.058)
0.021	(0.027)	0.05	(0.022)	0.09	(0.08)	0.018	(0.011)	0.008	(0.002)	0.017	(0.008)	0.054	(0.038)	0.013	(0.008)	0.083	(0.016)	0.029	(0.024)
0.28	(0.24)	0.11	(0.09)	0.060	(0.054)	0.121	(0.053)	0.016	(0.005)	0.065	(0.053)	0.14	(0.13)	0.071	(0.086)	0.129	(0.035)	0.067	(0.033)
–		–		–		0.179	(0.033)	2.67	(0.14)	–		0.122	(0.049)	–		0.096	(0.034)	–	
85.82		84.82		85.98		87.74		87.29		88.50		86.79		*82.85*		85.12		*85.78*	
Formula with 28-charge basis																			
2.86	(0.04)	2.70	(0.07)	2.78	(0.04)	3.20	(0.04)	3.17	(0.03)	2.84	(0.06)	3.22	(0.06)	*3.29*	*(0.05)*	3.29	(0.1)	*3.25*	*(0.03)*
b.d.l.		< 0.01		< 0.01		b.d.l.		b.d.l.	0.00	< 0.01		b.d.l.	0.00	*b.d.l.*	*0.00*	< 0.01		*<0.01*	
2.81	(0.03)	2.94	(0.07)	2.96	(0.05)	3.82	(0.05)	4.72	(0.04)	2.92	(0.1)	3.70	(0.06)	*4.84*	*(0.06)*	3.74	(0.12)	*4.88*	*(0.05)*
< 0.01		< 0.01		< 0.01		b.d.l.		b.d.l.	0.00	< 0.01		b.d.l.		*<0.01*		< 0.01		*<0.01*	
1.24	(0.02)	1.97	(0.05)	1.89	(0.05)	0.14	(0.02)	0.02	(0.006)	1.45	(0.1)	0.31	(0.07)	*0.02*	*(0.009)*	0.11	(0.02)	*0.03*	*(0.003)*
< 0.01		< 0.01		b.d.l.		< 0.01		b.d.l.	0.00	b.d.l.		b.d.l.		*<0.01*		b.d.l.		*b.d.l.*	
2.79	(0.06)	2.20	(0.09)	2.09	(0.04)	1.68	(0.09)	0.09	(0.02)	2.46	(0.07)	1.64	(0.07)	*0.09*	*(0.01)*	1.64	(0.14)	*0.13*	*(0.02)*
0.01	(0.005)	< 0.01		< 0.01		< 0.01		0.01	(0.003)	0.02	(0.005)	0.01	(0.01)	*0.04*	*(0.005)*	0.03	(0.002)	*0.01*	*(0.005)*
< 0.01		< 0.01		0.02	(0.02)	< 0.01		< 0.01		< 0.01		< 0.01		*<0.01*		0.01	(0.003)	*<0.01*	
0.04	(0.03)	0.01	(0.01)	< 0.01		0.01	(0.006)	< 0.01		< 0.01		0.02	(0.01)	*<0.01*		0.01	(0.004)	*<0.01*	
–		–		–		0.06	(0.01)	0.92	(0.04)	–		0.04	(0.02)	–		0.03	(0.01)	–	
9.76	(0.04)	9.85	(0.05)	9.75	(0.03)	8.93	(0.04)	8.93	(0.03)	9.70	(0.05)	8.96	(0.05)	*8.30*	*(0.02)*	8.87	(0.07)	*8.31*	*(0.01)*
5.76	(0.03)	5.85	(0.05)	5.75	(0.03)	4.93	(0.04)	4.93	(0.03)	5.70	(0.05)	4.96	(0.05)	*4.30*	*(0.02)*	4.87	(0.07)	*4.31*	*(0.02)*

https://doi.org/10.5194/ejm-35-831-2023

Table 2. Composition of micas measured in this study, averaged over the number of analyses given in the table. Lithium content has been verified as negligible but could not be quantified due to a beam size larger than crystal homogeneity (see "Analytical methods" for explanation). Dash: not measured, "b.d.l.": below detection limits.

Sample	LQ1		AR21-01		AR21-02		AR21-03			AR21-06B				AR21-07		AR21-16		AR21-24	
Mineral (n analyses)	Ill. mica ($n_{EPMA} = 5$)		Ill. mica ($n_{EPMA} = 6$)		Ill. mica ($n_{EPMA} = 4$)		Ill. mica ($n_{EPMA} = 7$)		Pg ($n_{EPMA} = 1$)	Ill. mica ($n_{EPMA} = 5$)		Pg (n_{EPMA} =2)		Ill. mica ($n_{EPMA} = 4$)		Ill. mica (n_{EPMA} =7)		Ill. mica (n_{EPMA} =2)	
Composition (ox. wt %)																			
SiO_2	46.48	(1.92)	44.58	(3.18)	45.88	(1.83)	45.75	(1.72)	49.82	47.79	(1.4)	48.50	(1.34)	48.68	(1.94)	49.69	(0.55)	45.38	(2.13)
TiO_2	0.35	(0.58)	0.65	(0.29)	0.64	(0.46)	1.32	(1.47)	0.05	0.15	(0.14)	b.d.l.		0.21	(0.24)	0.37	(0.15)	0.590	(0.084)
Al_2O_3	35.35	(1.59)	29.58	(1.41)	34.13	(1.42)	33.96	(1.68)	38.32	35.79	(0.69)	37.27	(1.93)	35.52	(2.32)	34.56	(0.76)	34.31	(2.57)
Cr_2O_3	0.057	(0.024)	b.d.l.		0.027	(0.024)	0.01	(0.04)	0.05	0.009	(0.014)	0.015	(0.008)	0.021	(0.009)	0.043	(0.013)	0.042	(0.001)
FeO	3.07	(1.96)	5.78	(1.9)	1.88	(0.73)	3.27	(2.02)	0.17	0.56	(0.13)	0.16	(0.17)	1.26	(1.72)	1.43	(0.33)	1.51	(1.1)
MnO	0.016	(0.063)	0.040	(0.028)	0.008	(0.031)	0.017	(0.033)	b.d.l.	0.001	(0.015)	0.039	(0.002)	0.014	(0.013)	b.d.l.		b.d.l.	
MgO	2.93	(1.65)	2.24	(0.58)	1.31	(0.89)	1.80	(0.96)	0.32	0.86	(0.22)	0.39	(0.28)	0.81	(0.26)	0.08	(0.02)	0.09	(0.06)
CaO	0.245	(0.063)	0.068	(0.039)	0.25	(0.16)	0.142	(0.039)	0.15	0.098	(0.078)	0.308	(0.056)	0.133	(0.081)	0.30	(0.055)	0.24	(0.06)
Na_2O	2.51	(0.54)	0.29	(0.14)	0.55	(0.32)	2.02	(0.62)	4.50	1.90	(1.01)	4.31	(0.69)	1.25	(1.11)	1.99	(0.35)	0.56	(0.14)
K_2O	4.14	(1.9)	9.65	(1.23)	9.38	(0.58)	5.39	(0.45)	3.18	6.55	(1.93)	1.76	(0.41)	6.65	(1.99)	4.84	(0.65)	7.02	(0.33)
Li_2O	–		–		–		–		–	–		–		–	0.055	(0.028)	–		
Total	95.14		92.87		94.06		93.68		96.55	93.71		92.75		94.56	94.72		90.97		
Formula with 22-charge basis																			
Si	3.04	(0.09)	3.12	(0.12)	3.09	(0.08)	3.06	(0.09)	3.14	3.15	(0.06)	3.15	(0.08)	3.18	(0.09)	3.22	(0.04)	3.10	(0.11)
Ti	0.02	(0.03)	0.03	(0.01)	0.03	(0.02)	0.07	(0.07)	< 0.01	< 0.01		< 0.01		0.01	(0.01)	0.02	(0.007)	0.03	(0.004)
Al	2.72	(0.1)	2.44	(0.12)	2.71	(0.09)	2.68	(0.11)	2.84	2.78	(0.06)	2.85	(0.09)	2.73	(0.12)	2.64	(0.04)	2.77	(0.15)
Cr	< 0.01		b.d.l.		< 0.01		< 0.01		< 0.01	< 0.01		b.d.l.		< 0.01	< 0.01		< 0.01		
Fe^{2+}	0.17	(0.1)	0.34	(0.1)	0.11	(0.04)	0.18	(0.1)	< 0.01	0.03	(0.006)	< 0.01		0.07	(0.09)	0.08	(0.02)	0.09	(0.06)
Mn	< 0.01		< 0.01		< 0.01		< 0.01		< 0.01	< 0.01		< 0.01		< 0.01	b.d.l.	0.00	b.d.l.		
Mg	0.29	(0.14)	0.23	(0.06)	0.13	(0.08)	0.18	(0.09)	0.03	0.08	(0.02)	0.04	(0.03)	0.08	(0.02)	0.14	(0.01)	0.13	(0.04)
Ca	0.02	(0.004)	< 0.01		0.02	(0.01)	0.01	(0.003)	b.d.l.	< 0.01		0.02	(0.004)	< 0.01	0.02	(0.004)	0.02	(0.004)	
Na	0.32	(0.06)	0.04	(0.02)	0.07	(0.04)	0.26	(0.07)	0.55	0.24	(0.11)	0.54	(0.08)	0.16	(0.14)	0.25	(0.05)	0.07	(0.02)
K	0.35	(0.14)	0.86	(0.1)	0.81	(0.05)	0.46	(0.04)	0.26	0.55	(0.15)	0.15	(0.03)	0.55	(0.15)	0.40	(0.05)	0.61	(0.03)
Li	–		–		–		–		–	–		–		–	0.01	(0.007)	–		
Cation sum	6.91	(0.11)	7.08	(0.11)	6.96	(0.06)	6.90	(0.08)	6.84	6.85	(0.13)	6.77	(0.07)	6.80	(0.15)	6.78	(0.05)	6.83	(0.05)
Interlayer sum	0.68	(0.14)	0.91	(0.1)	0.90	(0.06)	0.73	(0.09)	0.81	0.80	(0.18)	0.71	(0.09)	0.72	(0.21)	0.68	(0.07)	0.70	(0.04)
Octahedral sum	2.23	(0.1)	2.17	(0.07)	2.07	(0.05)	2.17	(0.07)	2.02	2.05	(0.05)	2.06	(0.03)	2.08	(0.08)	2.09	(0.03)	2.12	(0.05)

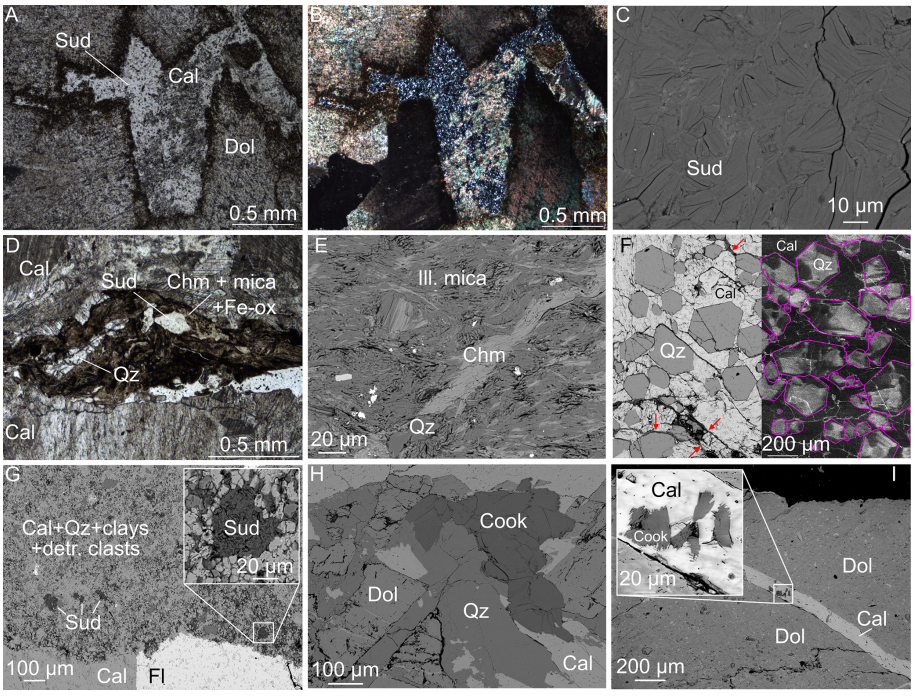

Figure 3. Mineral assemblages of the veins as observed in thin sections. Abbreviations are after Whitney and Evans (2009). **(a, b)** Optical microscopic views of sudoite co-crystallized with fine-grained calcite between dolomite crystals, in plane-polarized light and under crossed polars, sample AR21-10. **(c)** High-magnification BSE view of parts of sample LQ3a showing homogenous sudoite crystals. **(d)** Plane-polarized image of a dark layer in sample LQ1 (see Fig. 2c) containing organic matter, iron oxides, quartz, mica and chamosite in addition to a comparatively large crystal of sudoite, in coarse-grained calcite. **(e)** BSE view of interlayered chlorite–mica showing shearing and rotation of aggregates in sample AR21-3. Minor sulfides appear white. **(f)** Composite view of sample AR21-19 showing euhedral quartz in poikilitic calcite: BSE view left, SEM–cathodoluminescence right. Purple lines show quartz grain boundaries drawn from the corresponding BSE image. Red arrows indicate fine interstitial sudoite. **(g)** BSE view of sample AR21-21 showing sudoite in the finely grained host rock associated with quartz and calcite next to a fluorite–calcite–dolomite vein (see Fig. 2g); **(h)** BSE view of cookeite co-crystallizing with quartz and coarse-grained calcite, with dolomite in sample LQ2; **(i)** Cookeite-bearing calcite veinlet cross-cutting a large dolomite crystal in sample LQ3.

site types) and sudoite. The chamosite crystals show compositional variations well above analytical uncertainties, and Table 1 reports several chamosite compositions in some samples. This variability is attributed to growth zoning, but small crystal sizes and pervasive deformation (Figs. 2c–d, 3e) did not allow for further investigation.

Neither sudoite nor cookeite falls close to its ideal composition, and both are Al-depleted (Fig. 5b). Despite careful measurements, both show low cation sums in the range of 8.89–8.95 cations per formula unit (pfu). Cookeite is Mg-rich, and sudoite is Li-rich, in particular in sample LQ3.

4.3 Composition of mica

Illitic micas of the Aravis vein samples are K-deficient and contain Fe and Mg in the range of 0.12–0.57 cations pfu. At the resolution of FEG SEM imaging, the micas reported in Table 2 showed no sign of chlorite contamination. Figure 6 presents the dependency of interlayer sums on Si content (Fig. 6a) and octahedral sums (Fig. 6b). Pyrophyllitic substitution appears as a dominant exchange mechanism, without Tschermak substitution (negligible celadonite component in Fig. 6a). This is consistent with low-temperature crystallization (e.g. Battaglia, 2004; Abad et al., 2006) and low-pressure crystallization where Tschermak exchange is not expected in white mica. In agreement, incorporation of divalent cations is reflected by elevated octahedral sums (above 2 cations pfu, Fig. 6b) following di-trioctahedral substitution, often observed in low-temperature white mica (e.g. measurements of Abad et al., 2003, on very-low-grade pelites; experimental results of Vidal et al., 2012; modelling by Vidal and Dubacq, 2009).

5 Discussion

5.1 Origin of the fluids

The observed mineralogy indicates the presence of Li and F-rich fluids, in addition to Ca, Si, Mg and Al, less exotic elements in the host limestone of varying purity of the Aravis. Fluorite in the Aravis vein network has been linked to the

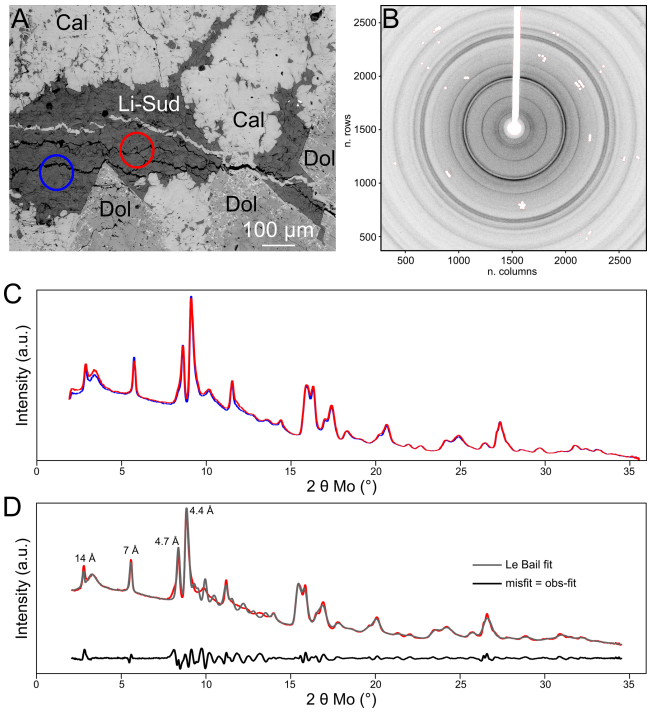

Figure 4. X-ray diffraction results for Li-rich sudoite in sample LQ3. **(a)** Back-scattered electron view of the measured areas (coloured circles). Each circle is 100 µm wide and encompasses about 95 % of the measured signal. **(b)** Raw diffraction pattern from the blue circle in **(a)**, hiding (in white) contributions from crystals identified as dolomite and from the beam stop and its holder. **(c)** Corresponding integrated diffraction patterns, in arbitrary units. Colours as in **(a)**. **(d)** Comparison of simulated diffraction pattern (grey, Le Bail method) to the second measurement (red, as in **a** and **c**). The misfit is shown in black.

Mont Blanc and Belledonne massifs by Pairis et al. (1992b), on the basis of rare earth content of the Aravis fluorite comparable to that of granites. But in these massifs, fluorite is rarely green and typically pink; it is associated with leaching of the granite during hydrothermal alteration following Miocene uplift, i.e. late in the collisional history (18–13 Ma; see Rossi et al., 2005). This timing is consistent with structuring and folding of the Aravis massif initiated in Palaeogene times and culminated in Miocene time during thrusting of the subalpine nappes (e.g. Pairis et al., 1992b, and references therein). However, the striking colour differences between Mont Blanc and Aravis fluorite indicate compositional differences, and presence of green fluorite in the Salève massif, likely isolated from Mont Blanc-derived fluids (presently ~ 60 km away), suggests different origin for the fluids. A simple alternative explanation is evaporite-derived fluids originating from the base of Prealpine nappes, mobilized during active tectonics, with the Salève massif sitting over a ramp at the extremity of the terranes overthrust by Prealpine nappes and cross-cut by NW–SE faults and calcite veins over 1 m in width (e.g. described by Charollais et al., 1998). Further analyses are needed, such as fluid inclusion salinity and trace element content of the vein minerals to better constrain the source of fluids.

5.2 Substitutions in cookeite and sudoite

Low cation sums in cookeite and sudoite, below 9 cations pfu, show that these analyses have no tri-trioctahedral component (10 cations). As shown by error propagation, these low totals are unlikely to originate solely from analytical uncertainties, especially from Li, which would be under-estimated by about 5000 ppm to explain 0.1 cation deficiency pfu in chlorite. Rather, low cation sums suggest that the M1 site of the TOT layer is empty and that the M4 site of the brucitic layer is not entirely filled (following the usual cation site distribution described in Vidal et al., 2001, and further detailed in Masci et al., 2019). The M1 and M4 sites of chlorite are preferential for vacancies and for univalent cations such as Li for symmetry reasons, located in the middle of hexagonal networks made by M2 octahedra in the TOT layer and M3 octahedra in the "brucitic" layer (e.g. Eggleton and Bailey, 1967; Aleksandrova et al., 1973; Bailey and Lister, 1989; Zheng and Bailey, 1997). Octahedral sums below 5 cations pfu exclude solid solution from a tri-trioctahedral end-member such as clinochlore (Fig. 5a–b).

Mg enrichment in cookeite and Li-enrichment in sudoite plead in favour of substitution towards a *virtual* Li-sudoite end-member of composition $\square LiMgAl_2(Si_4)O_{10}(OH)_8$ (Fig. 5a–b). This fictive end-member composition is attained from the sudoite end-member via the coupled substitution $Mg^{2+} + {}^{T}Al^{3+} = Li^{+} + Si^{4+}$; from cookeite it is reached via Tschermak substitution ($^{M}Al^{3+} + {}^{T}Al^{3+} = Mg^{2+} + Si^{4+}$).

Černý (1970) already noted that cookeite may include Mg above 1 wt % MgO, in addition to the more commonly observed substitution 3 $Li^{+} = Al^{3+}$ around the ideal formula unit. Merceron et al. (1988) compiled literature analyses showing compositions that were intermediate between cookeite and donbassite (Donb. in Fig. 5a, a di-dioctahedral chlorite end-member with formula unit $Al_{4.33}(AlSi_3)O_{10}(OH)_8$) and reported Li-rich donbassite. They argue in favour of the existence of a continuous solid solution between cookeite and donbassite and possibly with sudoite. Accordingly, Gonzalez-Lopez et al. (1993) report Li-rich chlorite with octahedral occupancy in the range of 4.5–4.7, i.e. between di-dioctahedral and di-trioctahedral (intermediate between donbassite and cookeite), from fluorite-bearing silicified limestone. In sudoite from the Aravis, octahedral sums are greater than 4.89 and the crystals are Mg-rich, excluding confusion with donbassite or tosudite, which are not observed. Substitution towards donbassite is not supported by the Aravis samples either, with all di-trioctahedral chlorite analyses falling out of the trian-

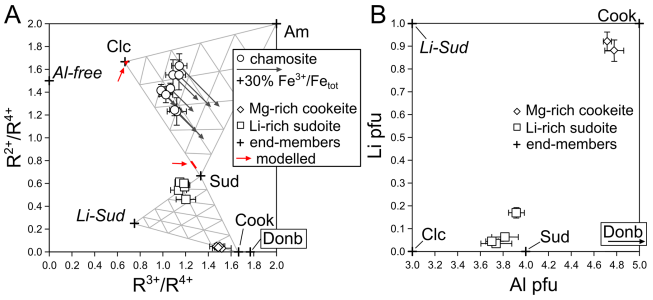

Figure 5. Chlorite composition, as in Table 1. **(a)** Cation ratios as measured with EPMA (from molar proportions). Triangles indicate end-member proportions every 20 %, in mixtures between clinochlore–amesite–sudoite (top) and between sudoite–cookeite–Li sudoite (bottom). Red domains indicated by arrows show modelled chlorite compositions. **(b)** Lithium and Al content of cookeite and sudoite, highlighting substitution towards a Li-sudoite component rather than towards cookeite. Substitution to clinochlore as the main mechanism to explain deviation of di-trioctahedral chlorite from ideal end-members is ruled out by low octahedral sums and incompatible cation ratios in **(a)**. Error bars are estimated from analytical uncertainties and variability in compositions.

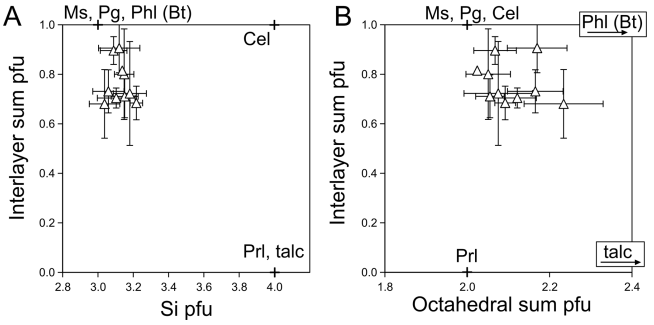

Figure 6. Mica composition, as in Table 2. Classical dioctahedral end-members are shown with crosses, with trioctahedral phlogopite and talc. Error bars propagate from analytical uncertainties and dispersion of compositions. **(a)** Si content, highlighting pyrophyllitic substitution. **(b)** Interlayer sum plotted against octahedral sum, showing presence of a trioctahedral component.

gles defined by sudoite–cookeite–donbassite or clinochlore–cookeite–donbassite in Fig. 5a and b.

5.3 Associated chamosite and mica

Chamosite associated with the vein network contains between $\sim 15\,\%$ and $\sim 40\,\%$ of a di-trioctahedral component (Fig. 5a). These values may be viewed as minimum estimates due to unknown, hard-to-assess iron speciation (presence of Fe^{3+} would increase this component if the anionic basis is unaffected by deprotonation; Masci et al., 2019). The Tschermak component (shifting analyses from clinochlore-like in Fig. 5a to amesite-like) varies over the same range as the di-trioctahedral component, showing that both substitutions are equally important in low-temperature chlorite. Uncertainties regarding formula units due to iron speciation indicate that the apparent sudoite proportion is a minimum value (Fig. 5a), assuming that the anionic basis is close to $O_{10}(OH)_8$. It is also noteworthy that the spread of composition is large and makes application of thermometers difficult. For example the thermometer of Bourdelle and Cathelineau (2015) is very sensitive to sudoite content and would yield temperatures ranging between about 125 and 300 °C. This compositional spread may be due to out-of-equilibrium crystallization or to evolution of the vein fluids caused by fractionation (as during Rayleigh fractionation). In any case, association of chamosite and sudoite with intermediate compositions is in favour of a solvus between di-trioctahedral and tri-trioctahedral chlorites. The solvus appears asymmetric with greater solubility of the sudoite component in chamosite than the other way around, consistent with earlier reports of associated chamosite and sudoite (e.g. Abad et al., 2003). Thermodynamic modelling has been carried out for conditions of 200 °C and 0.2 GPa in the C–CaO–FeO–MgO–Al_2O_3–SiO_2–H_2O system (C–CaFMASH) with the *MEEMUM* program of Perple_X (Connolly, 2009) using the only model encompassing di-trioctahedral, Fe–Mg and Tschermak substitutions in chlorite (Lanari et al., 2014); the dolomite–ankerite model of Holland and Powell (1998); and the database of Holland and Powell (1998). Silica, calcium carbonate and water were considered saturated. Bulk compositions span a range of Fe–Mg–Al–CO_2 contents (10 mol of FeO + MgO with variable X_{Mg} of 0.3, 0.5 and 0.7; 0–5 mol of Al_2O_3; and 0–10 mol of CO_2); results are detailed in the Supplement. Such modelling systematically results in chamosite associated with sudoite, with calcite, dolomite and quartz. However the predicted chlorite compositions differ strongly from observations (Fig. 5a): sudoite is predicted with high chamosite content (too high), X_{Mg} in the range of 0.8–1 (too high) and no Tschermak substitution (consistent with observations); chamosite is predicted with negligible Tschermak and di-trioctahedral substitutions (both too low) and X_{Mg} in the range of 0.6–0.8 (too high).

In mica, Tschermak substitution is secondary to pyrophyllitic and di-trioctahedral substitution again. Application of the simple thermometer derived by Battaglia (2004) on the basis of these substitutions to illitic mica analyses of Table 2 yielded a median value at 190 °C, perfectly consistent with thermal constraints cited above but with high variability in individual estimates (50 °C standard deviation over the dataset). Other thermometric estimation methods performed similarly or worse, and equilibration with chamosite could not be modelled using multi-equilibrium models (e.g. as in Vidal et al., 2006). Ubiquitous presence of carbonates may lead to suggesting low water activity, but crystallization conditions are well in the two-phase region of the H_2O–CO_2 phase, where CO_2 does not lower water activity significantly (Dubacq et al., 2013).

To summarize, chamosite and mica from the low-temperature Aravis vein network show expected compositions, similar to literature reports in comparable settings, but thermodynamic modelling remains ineffective at reproducing equilibrium between these minerals. It may be that thermodynamic models, in particular solid solution models, are to blame and that thermodynamic modelling should include di-trioctahedral substitution in chlorite and mica and pyrophyllitic substitution in mica to approach the compositions observed in the Aravis vein network. Attempts to neglect these substitutions will lead either to misestimation of Tschermak substitution to fit, for example, Si/Al ratios or to incorrect stability conditions. However, compositional variations indicate that equilibrium was not fully attained in the veins. Metastability is not a surprising feature under the peak conditions of the Aravis massif; for example Abad et al. (2003) documented how phyllosilicates show increasingly homogenous composition from diagenesis to greenschist-facies conditions. Whether compositional variations in the Aravis vein network are obtained through out-of-equilibrium crystallization or under local equilibrium with open-system behaviour is unclear as univocal textural evidence is missing.

6 Conclusions

Co-existence of Li-rich sudoite with Mg-rich cookeite points to limited solid solution between the two phases; however the variability between sudoite analyses suggests that equilibrium with cookeite was not reached during crystallization of all the Li-rich sudoite grains. Because it appears that Li-rich sudoite is homogenous when filling cavities (e.g. Fig. 3a–b) but heterogeneous above the sample scale, it is difficult to assess with certainty which could have equilibrated with the cookeite found scattered in the veins. Crystallization of the chlorite assemblage during emplacement of the vein network is hypothesized to have taken place during or just after maximum burial (7 km, 190 °C), which is consistent with crystallization temperatures reported for sudoite and cookeite (Černý, 1970; Merceron et al., 1988; Gonzalez-Lopez, 1993).

The chlorite assemblage from the Aravis vein network is also in favour of limited solid solution between chamosite and di-trioctahedral chlorite. At first glance, this is in support of thermodynamic models using solvi (e.g. Vidal et al., 2006; Lanari et al., 2014) but the thermodynamic status of substitutions between di-dioctahedral, di-trioctahedral and tri-trioctahedral chlorites remains enigmatic. The continuity between donbassite and cookeite (Merceron et al., 1988), if not due to metastability, may be due to the presence of Li. Lithium combines low charge – hence mobility – with a radius compatible with incorporation into octahedral layers (at 0.76 Å, slightly above Mg^{2+} at 0.72 Å, much lower than Na^{+} and K^{+} at 1.02 and 1.38 Å respectively with the radii from Shannon, 1976), which may ease breaking symmetry relations within octahedral layers, explaining greater solubility between donbassite and cookeite than between chamosite and sudoite (here remaining much less Li-rich than cookeite).

The presence of Li in chlorite may be more common than generally reported because Li is easy to miss with traditional electron microscopy, and as little as 1 wt % Li_2O represents about 0.35 Li atoms pfu in sudoite. The fact that there is no known Li-rich tri-trioctahedral chlorite end-member may reflect this, in addition to identification difficulties of likely small, white or pale crystals (see e.g. Hazen, 2015). Identifying dilute crustal reservoirs of Li and modelling the phase relations of low-temperature phyllosilicates call for renewed systematic studies of their light-element content and particularly in low-grade chlorite.

Data availability. No data sets were used in this article.

Supplement. The supplement related to this article is available online at: https://doi.org/10.5194/ejm-35-831-2023-supplement.

Author contributions. BD, GB and MW carried out the main fieldwork campaign and the chemical analyses. BB carried out the X-ray diffraction experiments with the co-authors and performed the associated modelling. The manuscript was prepared by BD and reviewed and corrected by the co-authors.

Competing interests. The contact author has declared that none of the authors has any competing interests.

Disclaimer. Publisher's note: Copernicus Publications remains neutral with regard to jurisdictional claims in published maps and institutional affiliations.

Acknowledgements. This study benefited from the help of Benoît Caron and Julie Noël for LA ICP-MS/MS measurements, Nicolas Rividi and Michel Fialin for EPMA, and Omar Boudouma for SEM imagery. Anne Verlaguet is thanked for kindly providing cookeite samples. Authors are grateful to the associate editor Chiara Groppo and to the anonymous reviewer for their detailed and constructive reviews. Aline and Jean-Paul Govin are thanked for waiting while Benoît Dubacq looked at yet another rock.

Financial support. This research has been supported by CNRS-INSU via its TelluS SYSTER programme (attributed to Guillaume Bonnet and Benoît Dubacq).

Review statement. This paper was edited by Chiara Groppo and reviewed by Chiara Groppo and one anonymous referee.

References

Abad, I., Nieto, F., Peacor, D. R., and Velilla, N.: Prograde and retrograde diagenetic and metamorphic evolution in metapelitic rocks of Sierra Espuña (Spain), Clay. Clay Miner., 38, 1–23, https://doi.org/10.1180/0009855033810074, 2003.

Abad, I., Nieto, F., Gutierrez-Alonso, G., do Campo, M., Lopez-Munguira, A., and Velilla, N.: Illitic substitution in micas of very low-grade metamorphic clastic rocks, Eur. J. Miner., 18, 59–69, https://doi.org/10.1127/0935-1221/2006/0018-0059, 2006.

Aleksandrova, V. A., Drits, V. A., and Sokolova, G. V.: Crystal structure of ditrioctahedral chlorite, Sov. Phys. Crystallogr., 18, 50–53, 1973.

Bailey, S. and Lister, J.: Structures, compositions, and X-ray-diffraction identification of dioctahedral chlorites, Clay. Clay Miner., 37, 193–202, https://doi.org/10.1346/CCMN.1989.0370301, 1989.

Battaglia, S.: Variations in the chemical composition of illite from five geothermal fields: a possible geothermometer, Clay Miner., 39, 501–510, https://doi.org/10.1180/0009855043940150, 2004.

Bellahsen, N., Mouthereau, F., Boutoux, A., Bellanger, M., Lacombe, O., Jolivet, L., and Rolland, Y.: Collision kinematics in the western external Alps, Tectonics, 33, 1055–1088, https://doi.org/10.1002/2013TC003453, 2014.

Bourdelle, F., Parra, T., Beyssac, O., Chopin, C., and Vidal, O.: Clay minerals as geo-thermometer: A comparative study based on high spatial resolution analyses of illite and chlorite in Gulf Coast sandstones (Texas, U.S.A.), Am. Mineral., 98, 914–926, https://doi.org/10.2138/am.2013.4238, 2013a.

Bourdelle, F., Parra, T., Chopin, C., and Beyssac, O.: A new chlorite geothermometer for diagenetic to low-grade metamorphic conditions, Contrib. Mineral. Petr., 165, 723–735, https://doi.org/10.1007/s00410-012-0832-7, 2013b.

Bourdelle, F. and Cathelineau, M.: Low-temperature chlorite geothermometry: a graphical representation based on a T–R2+–Si diagram, Eur. J. Mineral., 27, 617–626, https://doi.org/10.1127/ejm/2015/0027-2467, 2015.

Butler, R. W. H.: Hydrocarbon maturation, migration and tectonic loading in the Western Alpine foreland thrust belt Geol. Soc., London, Spec. Publ., 59, 227–244, https://doi.org/10.1144/GSL.SP.1991.059.01.15, 1991.

Cathelineau, M.: Cation Site Occupancy in Chlorites and Illites as a Function of Temperature, Clay. Clay Miner., 23, 471–485, 1988.

Černý, P.: Compositional variations in cookeite, Can. Mineral., 10, 636–647, 1970.

Charollais, J., Plancherel, R., Monjuvent, G., and Debelmas, J.: Notice explicative, Carte géol. France (1/50000), feuille Annemasse (654) – Orléans: Bureau de recherches géologiques et minières, 130 pp., ISBN 2-7159-1654-X, 1998.

Connolly, J. A. D.: The geodynamic equation of state: What and how, Geochem. Geophy. Geosy., 10, Q10014, https://doi.org/10.1029/2009GC002540, 2009.

Deville, E. and Sassi, W.: Contrasting thermal evolution of thrust systems: An analytical and modeling approach in the front of the western Alps, AAPG Bull., 90, 887–907, https://doi.org/10.1306/01090605046, 2006.

Dubacq, B., Vidal, O., and De Andrade, V.: Dehydration of dioctahedral aluminous phyllosilicates: thermodynamic modelling and implications for thermobarometric estimates, Contrib. Mineral. Petr., 159, 159–174, https://doi.org/10.1007/s00410-009-0421-6, 2010.

Dubacq, B., Bickle, M. J., and Evans, K. A.: An activity model for phase equilibria in the H_2O-CO_2-NaCl system, Geochim. Cosmochim. Ac., 110, 229–252, https://doi.org/10.1016/j.gca.2013.02.008, 2013.

Dowty, E.: Crystal structure and crystal growth: II. sector zoning in minerals, Am. Miner., 61, 460–469, 1976.

Dumont, T., Champagnac, J.-D., Crouzet, C., and Rochat, P.: Multistage shortening in the Dauphiné zone (French Alps): the record of Alpine collision and implications for pre-Alpine restoration, Swiss J. Geosci., 101, 89–110, https://doi.org/10.1007/s00015-008-1280-2, 2008.

Eggleton, R. A. and Bailey, S. W.: Structural aspects of dioctahedral chlorite, Am. Mineral., 52, 673–689, 1967.

Féraud, J.: La fluorine des Aravis, Bulletin du club de Minéralogie de Chamonix, du Mont Blanc et des Alpes du Nord, Bulletin du club de Minéralogie de Chamonix, 71, 51–60, 2021.

Gonzalez-Lopez, J. M., Subias Perez, I., Fernandez-Nieto, C., and Gonzalez, I. F.: Lithium-bearing hydrothermal alteration phyllosilicates related to Portalet fluorite ore (Pyrenees, Huesca, Spain), Clay. Clay Miner., 28, 275–283, 1993.

Hammersley, A. P.: FIT2D: a multi-purpose data reduction, analysis and visualization program, J. Appl. Crystallogr., 49, 646–652, https://doi.org/10.1107/S1600576716000455, 2016.

Hazen, R. M., Hystad, G., Downs, R. T., Golden, J. J., Pires, A. J., and Grew, E. S.: Earth's "missing" minerals, Am. Mineral., 100, 2344–2347, https://doi.org/10.2138/am-2015-5417, 2015.

Holland, T. J. B. and Powell, R.: An internally consistent thermodynamic data set for phases of petrological interest, J. Metamorp. Geol., 16, 309–343, https://doi.org/10.1111/j.1525-1314.1998.00140.x, 1998.

Holland, T. and Powell, R.: Activity-composition relations for phases in petrological calculations: an asymmetric multicomponent formulation, Contrib. Mineral. Petr., 145, 492–501, https://doi.org/10.1007/s00410-003-0464-z, 2003.

Inoue, A., Meunier, A., Patrier-Mas, P., Rigault, C., Beaufort, D., and Vieillard, P.: Application of chemical geothermometry to low-temperature trioctahedral chlorites, Clay. Clay Miner., 57, 371–382 https://doi.org/10.1346/CCMN.2009.0570309, 2009.

Lacroix, A.: Minéralogie de la France et de ses colonies : description physique et chimique des minéraux, étude des conditions géologiques de leurs gisements. Eds: Librairie Polytechnique, Baudry et Cie (Paris), 2, p. 799, 1896.

Lanari, P., Wagner, T., and Vidal, O.: A thermodynamic model for di-trioctahedral chlorite from experimental and natural data in the system MgO-FeO-Al_2O_3-SiO_2-H_2O: applications to P–T sections and geothermometry, Contrib. Mineral. Petr., 167, 968, https://doi.org/10.1007/s00410-014-0968-8, 2014.

Mangenot, X., Deçoninck, J.-F., Bonifacie, M., Rouchon, V., Collin, P.-Y., Quesne, D., Gasparrini, M., and Sizun, J.-P.: Thermal and exhumation histories of the northern subalpine chains (Bauges and Bornes – France): Evidence from forward thermal modeling coupling clay mineral diagenesis, organic maturity and carbonate clumped isotope ($\Delta 47$) data, Basin Res., 31, 361–379, https://doi.org/10.1111/bre.12324, 2019.

Masci, L., Dubacq, B., Verlaguet, A., Chopin, C., De Andrade, V., and Herviou, C. : A XANES and EPMA study of Fe^{3+} in chlorite: Importance of oxychlorite and implications for cation site

distribution and thermobarometry, Am. Mineral., 104, 403–417, https://doi.org/10.2138/am-2019-6766, 2019.

Merceron, T., Inoue, A., Bouchet, A., and Meunier, A.: Lithium-bearing donbassite and tosudite from Echassieres, Massif Central, France, Clay. Clay Miner., 36, 39–46 https://doi.org/10.1346/CCMN.1988.0360106, 1988.

Meunier, A. and Velde, B.: Solid-Solutions, in: I/S Mixed-Layer Minerals And Illite, Am. Miner., 74, 1106–1112, 1989.

Moss, S.: Organic maturation in the French Subalpine Chains: regional differences in burial history and the size of tectonic loads, J. Geol. Soc., London, 149, 503–515, https://doi.org/10.1144/gsjgs.149.4.0503, 1992.

Muirhead, D. K., Bond, C. E., Watkins, H., Butler, R. W. H., Schito, A., Crawford, Z., and Marpino, A.: Raman spectroscopy: an effective thermal marker in low temperature carbonaceous fold-thrust belts, Geol. Soc., London, Spec. Publ., 490, 135–151, https://doi.org/10.1144/SP490-2019-27, 2020.

Pairis, J. L., Pairis, B., Bellière, J., Rosset, J., Détraz, H., Muller, A., Muller, D., Villars, F., Mennessier, G., Charollais, J., Kindler, P., Pierre, X., and Uselle, J. P.: Carte géol. France (1/50000), feuille Cluses, Bureau de recherches géologiques et minières, Orléans, Map 679, 1992a.

Pairis, J. L., Bellière J., and Rosset J.: Notice explicative, Carte géol. France (1/50000), feuille Cluses (679), Bureau de recherches géologiques et minières, Orléans, p. 89., ISBN 2-7159-1679-5, 1992b.

Pouchou, J.-L., Pichoir, F.: Heinrich, K. F. J., and Newbury, D. E. (Eds.): Quantitative Analysis of Homogeneous or Stratified Microvolumes Applying the Model "PAP", in: Electron Probe Quantitation, Springer US, 31–75, https://doi.org/10.1007/978-1-4899-2617-3_4, 1991.

Rodríguez-Carvajal, J.: Recent Advances in Magnetic Structure Determination by Neutron Powder Diffraction, Physica B: Condensed Matter, 192, 55–69, https://doi.org/10.1016/0921-4526(93)90108-I, 1993.

Rosset, J.: Description géologique de la chaîne des Aravis entre Cluses et le col des Aravis (Haute-Savoie), PhD thesis, Faculté des Sciences de l'Université de Grenoble, 89 pp., 1954.

Rossi, M., Rolland, Y., Vidal, O., and Cox, S. F.: Geochemical variations and element transfer during shear-zone development and related episyenites at middle crust depths: insights from the Mont Blanc granite (French – Italian Alps) Geol. Soc., London, Spec. Pub., 245, 373–396, https://doi.org/10.1144/GSL.SP.2005.245.01.18, 2005.

Shannon, R. D.: Revised effective ionic radii and systematic studies of interatomic distances in halides and chalcogenides, Acta Crystallogr. Section A, 32, 751–767, https://doi.org/10.1107/S0567739476001551, 1976.

Soret, F.: Rapport sur les minéraux rares ou offrant des cristallisations nouvelles, observés dans la collection du Musée académique de Genève, Mémoires de la société de physique et d'histoire naturelle de Genève, 1, 465–500, 1822.

Van Hinsberg, V. J., Schumacher, J. C., Kearns, S., Mason, P. R., and Franz, G.: Hourglass sector zoning in metamorphic tourmaline and resultant major and trace-element fractionation, Am. Miner., 91, 717–728, https://doi.org/10.2138/am.2006.1920, 2006.

Verlaguet, A., Goffé, B., Brunet, F., Poinssot, C., Vidal, O., Findling, N., and Menut, D. : Metamorphic veining and mass transfer in a chemically closed system: a case study in Alpine metabauxites (western Vanoise), J. Metamorph. Geol., 29, 275–300, https://doi.org/10.1111/j.1525-1314.2010.00918.x, 2011.

Vidal, O., Parra, T., and Trotet, F.: A Thermodynamic Model for Fe-Mg Aluminous Chlorite Using Data from Phase Equilibrium Experiments and Natural Pelitic Assemblages in the 100° to 600 °C, 1 to 25 kb Range, Am. J. Sci., 301, 557–592, https://doi.org/10.2475/ajs.301.6.557, 2001.

Vidal, O., De Andrade, V., Lewin, E., Munoz, M., Parra, T., and Pascarelli, S.: P-T-deformation-Fe^{3+}/Fe^{2+} mapping at the thin section scale and comparison with XANES mapping: application to a garnet-bearing metapelite from the Sambagawa metamorphic belt (Japan), J. Metamorph. Geol., 24, 669–683, https://doi.org/10.1111/j.1525-1314.2006.00661.x, 2006.

Vidal, O. and Dubacq, B.: Thermodynamic modelling of clay dehydration, stability and compositional evolution with temperature, pressure and H_2O activity, Geochim. Cosmochim. Ac., 73, 6544–6564, https://doi.org/10.1016/j.gca.2009.07.035, 2009.

Vidal, O., Baldeyrou, A., Beaufort, D., Fritz, B., Geoffroy, N., and Lanson, B.: Experimental Study of the Stability and Phase Relations of Clays at High Temperature in a Thermal Gradient, Clay. Clay Miner., 60, 200–225, https://doi.org/10.1346/CCMN.2012.0600209, 2012.

Walker, J. R. and Bish, D. L.: Application of Rietveld Refinement Techniques to a Disordered IIb Mg-Chamosite, Clay. Clay Miner., 40, 319–322, https://doi.org/10.1346/CCMN.1992.0400311, 1992.

Walshe, J. L.: A six-component chlorite solid solution model and the conditions of chlorite formation in hydrothermal and geothermal systems, Econ. Geol., 81, 681, https://doi.org/10.2113/gsecongeo.81.3.681, 1986.

White, R. W., Powell, R., Holland, T. J. B., Johnson, T. E., and Green, E. C. R.: New mineral activity-composition relations for thermodynamic calculations in metapelitic systems, J. Metamorph. Geol., 32, 261–286, https://doi.org/10.1111/jmg.12071, 2014.

Whitney, D. L. and Evans, B. W.: Abbreviations for names of rock-forming minerals, Am. Mineral., 95, 185–187, https://doi.org/10.2138/am.2010.3371, 2009.

Zheng, H. and Bailey, S. W.: Refinement of the cookeite "r" structure, Am. Miner., 82, 1007–1013, 1997.